Journal of Alloys and Compounds 1039 (2025) 183052

Contents lists available at ScienceDirect

Journal of Alloys and Compounds

journal homepage: www.elsevier.com/locate/jalcom

Rapid reversible hydrogen storage in $2LiBH_4$-MgH_2 composite achieved by graphene-wrapped niobium oxide nanoparticles

Chaoqun Li, Ying Ding, Xiaoyue Zhang, Xuechun Hu, Guanglin Xia *

College of Smart Materials and Future Energy, Fudan University, Shanghai 200433, China

ARTICLE INFO

Keywords:
Hydrogen storage
Graphene-wrapped
Niobium oxide nanoparticles
MgB_2 nucleation
Reactive hydride composite
Catalytic mechanism

ABSTRACT

$2LiBH_4$-MgH_2 composite that undergoes re-hydrogenation under relatively mild conditions achieves a high reversible capacity of 10.8 wt%, positioning it as a promising material for hydrogen storage. However, the slow kinetics due to the difficult nucleation of MgB_2 serve as the critical step that limits the hydrogen desorption rate, which hinders its commercial application. Therefore, a low-crystallinity graphene-wrapped Nb_2O_5 nanoparticles (Nb_2O_5@G) is designed to *in-situ* synthesize NbB_2 nanoparticles for accelerating the nucleation and growth of MgB_2. Moreover, upon reducing the particle size to the nanometer scale, Nb_2O_5 is more easily reduced to a lower valence state, which accelerates the formation of NbB_2 and further shortens the incubation time of MgB_2. As a result, under the catalysis of Nb_2O_5@G, the $2LiBH_4$-MgH_2 composite achieves a desorption amount of 9.5 wt% H_2 within only 100 min, outperforming the commercial Nb_2O_5 catalyzed composite by 8 times. More importantly, stable reversible hydrogen storage with a capacity of 9.3 wt% and a capacity retention of 98 % after 10 cycles could be achieved for $2LiBH_4$-MgH_2 composite under the catalysis of Nb_2O_5@G.

1. Introduction

Hydrogen energy is increasingly recognized as a cornerstone of future clean and sustainable energy systems, owing to its high energy density and environmentally benign combustion products [1,2]. Nevertheless, its practical application is currently limited by the absence of safe, efficient, and reversible hydrogen storage technologies [3,4]. Among various approaches to hydrogen storage, solid-state materials offer significant advantages, including high volumetric energy density, enhanced operational safety, and adaptability to different scenarios compared with conventional methods of storing hydrogen as high-pressure gas or cryogenic liquid [5–9]. Despite of their promise, the challenges of high operating temperatures, sluggish kinetics, and poor reversibility continue to limit the widespread adoption of solid-state hydrogen storage materials.

Magnesium hydride (MgH_2) and lithium borohydride ($LiBH_4$) are among the most extensively studied hydrides due to their exceptionally high theoretical hydrogen capacities of 7.6 wt% and 18.5 wt%, respectively. MgH_2 features relatively low cost, abundance, and reversible hydrogen storage properties, yet its slow hydrogenation/dehydrogenation kinetics and high decomposition temperature (~300 °C) remain significant barriers [10–12]. $LiBH_4$, while possessing one of the highest hydrogen storage capacities among metal hydrides, suffers from an even higher decomposition temperature (~450 °C) and poor reversibility [13,14]. To address these limitations, the combination of MgH_2 and $LiBH_4$ into a $2LiBH_4$-MgH_2 composite has emerged as a promising strategy. This composite exploits the synergistic thermodynamic and kinetic interactions between two hydrides, lowering the overall reaction enthalpy. During dehydrogenation, a hydrogen back pressure of 3–5 bar is required to ensure the completion of the following two reaction steps (Eqs. (1) and (2)), facilitating the formation of MgB_2 and maintaining reaction reversibility [15,16]:

$$2LiBH_4 + MgH_2 \leftrightarrow 2LiBH_4 + Mg + H_2 \quad (1)$$

$$2LiBH_4 + Mg + H_2 \leftrightarrow 2LiH + MgB_2 + 4H_2 \quad (2)$$

However, the rate-determining step of MgB_2 formation and the high temperature required for this reaction (~350–400 °C) continue to limit the practical utility of this composite [17].

Catalyst modification has emerged as an effective strategy for addressing the slow kinetics of hydrogen storage materials [18–20]. In terms of the $2LiBH_4$-MgH_2 system, ideal catalysts must fulfill dual functions: facilitating the breaking of B-H bonds during dehydrogenation, and providing effective nucleation sites to guide the crystallization

* Corresponding author.
E-mail address: xiaguanglin@fudan.edu.cn (G. Xia).

https://doi.org/10.1016/j.jallcom.2025.183052
Received 20 June 2025; Received in revised form 11 August 2025; Accepted 13 August 2025
Available online 14 August 2025

of intermediate phases. Recent studies have demonstrated that the introduction of catalysts capable of facilitating the formation of layered metal borides is an effective way to improve reversible hydrogen storage of $2LiBH_4$-MgH_2 system [21–25], as these structures can serve as preferential nucleation templates for the formation of MgB_2. For example, under the catalysis of NbB_2, which shares a similar crystal structure with MgB_2[26], $2LiBH_4$-MgH_2 system could rapidly release 7.55 wt% H_2 at 320 °C [27]. Building nanostructured catalysts is an effective approach to enhance their catalytic effect in promoting hydrogen storage performance of $2LiBH_4$-MgH_2 composite [16,28–32]. In a previous work [25], under the catalysis of amorphous VB_2 nanoparticles, $2LiBH_4$-MgH_2 composite realized complete dehydrogenation within 2 h, half the time required for that catalyzed by commercial VB_2. The decrease in particle size of catalysts down to a nanoscale size could effectively improve the nucleation efficiency of MgB_2, thereby contributing to the enhancement of the reversible hydrogen storage performance in $2LiBH_4$-MgH_2 composite. Therefore, there is a critical need to develop advanced catalysts capable of providing nanoscale nucleation sites to further enhance the catalytic efficiency of $2LiBH_4$-MgH_2 composite for realizing rapid reversible hydrogen storage.

In this study, we present the development of a graphene-wrapped nano niobium oxide (Nb_2O_5@G) catalyst, which has been shown to significantly accelerate the dehydrogenation rate of $2LiBH_4$-MgH_2 system towards high-capacity reversible hydrogen storage. The slow formation of MgB_2 is addressed by using ultrafine nanoparticle Nb_2O_5, which, in combination with graphene as a support that facilitates the nanoconfinement of the thus-formed catalyst [33–36] and $2LiBH_4$-MgH_2 composite. The reaction between $LiBH_4$ and Nb_2O_5 leads to *in-situ* formation of nanostructured NbB_2 that exhibits similar lattice structure to MgB_2 with low *d*-value mismatch, which significantly reduces the formation energies of Mg and B layers by 27.42 kJ·mol^{-1} and 85.96 kJ·mol^{-1}, respectively. The synergistic effects of graphene and NbB_2 enhance the kinetics of MgB_2 formation, thereby eliminating the incubation times and consequently reducing dehydrogenation temperatures. As a result, the $2LiBH_4$-MgH_2 composite releases 9.5 wt% hydrogen within 125 min during the first dehydrogenation cycle at 400 °C under the catalysis of Nb_2O_5@G. In contrast, the commercial Nb_2O_5-catalyzed $2LiBH_4$-MgH_2 composite requires over 15 h for complete dehydrogenation. More importantly, the Nb_2O_5@G-catalyzed $2LiBH_4$-MgH_2 composite achieves complete dehydrogenation in just 90 min during subsequent cycles, maintaining a hydrogen storage capacity of 9.3 wt% over 10 cycles.

2. Experimental section

2.1. Synthesis of Nb_2O_5@G:

100 mg of $NbCl_5$ was dissolved in 20 mL of anhydrous ethanol under stirring in an ice-water bath to obtain solution A. Simultaneously, 6.4 mL of graphene oxide (GO) dispersion (2 mg·mL^{-1}) was sonicated in 20 mL anhydrous ethanol to form solution B. Solution B was then added dropwise to solution A while maintaining stirring in the ice-water bath. Afterward, 1 mL of oleylamine was added, and the mixture was heated to 75 °C and stirred rapidly for 6 h. The resulting product was washed with ethanol and deionized water and centrifuged. Subsequently, 120 mg of sodium ascorbate and 8 mL of deionized water were added and sonicated, followed by heating at 100 °C for 2 h to reduce the graphene oxide. The thus-obtained sample was then washed with deionized water, centrifuged, freeze-dried, and placed in a tube furnace for heating at 600 °C for 3 h with a rate of 5 °C·min^{-1}. The final product obtained was Nb_2O_5@G.

2.1.1. Synthesis of the $2LiBH_4$-MgH_2-Nb_2O_5@G composite

Nb_2O_5@G, $LiBH_4$, and MgH_2 were weighed in varying proportions and thoroughly mixed before being transferred to a stainless-steel high-pressure ball milling jar. Steel balls were added at a ball-to-material ratio of 120:1, and the jar was sealed and subjected to 50 bar of hydrogen. The milling process was carried out for 10 h, with a milling cycle of 15 min followed by a 5-minute pause to prevent localized overheating and hydrogen loss. All weighing and handling of materials were performed in an argon-filled glove box with oxygen and moisture levels below 0.1 ppm.

2.2. Characterization

The phase composition of the powdered samples was characterized using X-ray diffraction (XRD) with a Bruker D8 Advance diffractometer and Cu Kα radiation (λ = 1.5418 Å). To minimize air-induced reactions, an amorphous tape was applied to the samples, resulting in a broad peak near 2θ ≈ 20°. Sample morphology was observed *via* field-emission scanning electron microscopy (FE-SEM, ZEISS Gemini 300) and transmission electron microscopy (TEM, JEOL JEM-2100F). Surface chemical analysis was performed using X-ray photoelectron spectroscopy (XPS, ThermoFisher ESCALAB 250Xi), operating at an analysis chamber pressure of 8 × 10^{-10} Pa, with an Al Kα excitation source ($h\nu$ = 1486.6 eV), a working voltage of 12.5 kV, and filament current of 16 mA. Signals were accumulated over 5–10 cycles, with a pass energy of 20 eV and a step size of 0.1 eV, and charge correction was applied using C1*s* = 284.60 eV. To prevent air contamination, air-sensitive $2LiBH_4$-MgH_2 composites were transferred with a custom-designed vessel in a glovebox. Chemical bonding was examined using fourier-transform infrared spectroscopy (FT-IR, Magna-IR 550 II, Nicolet), where the powdered samples were mixed with KBr, pressed into translucent pellets, and analyzed.

2.3. Density function theory calculations

First-principles density functional theory (DFT) calculations were conducted utilizing the projector augmented wave (PAW) method [37] within the Vienna Ab initio Simulation Package (VASP). To describe the electronic exchange-correlation effects, the Perdew-Burke-Ernzerhof (PBE) functional under the generalized gradient approximation (GGA) was adopted [38–40]. Dispersion forces were accounted for by applying Grimme's DFT-D3 van der Waals correction [41]. Since the deposition of the B atomic layer leads to an asymmetric structure along the top and bottom surfaces, a dipole moment correction in the *z*-direction was applied during the calculations. Calculations employed a plane-wave cutoff energy of 550 eV and a (4 × 4 × 1) *Γ*-centered *k*-point grid. The Gaussian smearing method was used with a width parameter of 0.05 eV, and all computations were spin-polarized. Structural optimizations proceeded until atomic forces and total energy converged to thresholds of less than 0.02 eV·Å^{-1} and 1 × 10^{-5} eV, respectively.

3. Results and discussion

As shown in Fig. 1**a**, the synthesis of Nb_2O_5@G involved a straightforward procedure that entailed heating and stirring, followed by freeze-drying and high-temperature calcination. A weak characteristic peak of Nb_2O_5 (PDF#30–0873) [42] was observed in the X-ray diffraction (XRD) pattern (Fig. 1**b**). The binding energies of 207.3 eV and 210.0 eV in the high-resolution Nb 3*d* X-ray photoelectron spectroscopy (XPS) spectrum (Fig. 1**c**) further confirm the successful formation of Nb_2O_5[43]. Scanning electron microscopy (SEM) image (Fig. 1**d**) demonstrates that the particle size of Nb_2O_5 is in the range of 10–20 nm, with uniform distribution of nanoparticles on the surface of graphene. As shown in Fig. 1**e**, the interplanar spacing of Nb_2O_5 measured by high-resolution transmission electron microscopy (HRTEM) is 0.314 nm[42], which corresponds to the characteristic peaks observed in the XRD spectrum. Energy dispersive spectroscopy (EDS) mapping (Fig. 1**f**) provides further evidence of the uniform dispersion of Nb elements across the graphene.

To evaluate the catalytic effect of Nb_2O_5@G on the hydrogen storage performance of $2LiBH_4$-MgH_2 (denoted as LBMH) composite, the

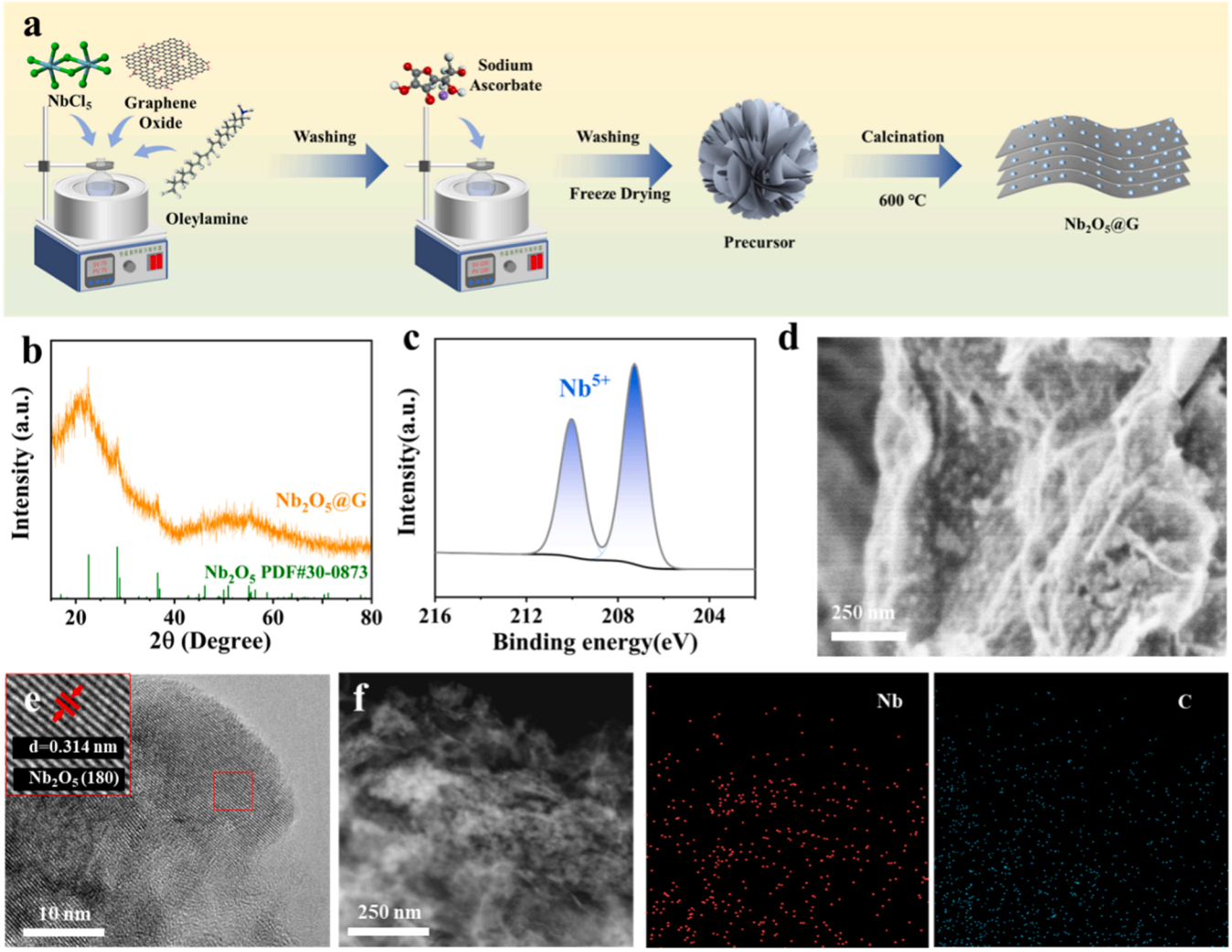

Fig. 1. Preparation and characterization of Nb_2O_5@G. (a) Preparation process of Nb_2O_5@G. (b) XRD patterns, (c) FTIR spectra, (d) SEM image, (e) HRTEM image, (f) TEM image, and relative EDS elemental mapping images of Nb and C of Nb_2O_5@G.

composite was ball-milled with Nb_2O_5@G with mass fractions of 4 wt%, 7 wt%, and 10 wt% (All weight percentages mentioned in the manuscript refer to the total mass of the composite, including $LiBH_4$, MgH_2, and the catalyst, without excluding the mass of support materials such as graphene.). Isothermal dehydrogenation experiments were conducted at 400 °C under a hydrogen pressure of 4 bar, and the results are presented in Fig. S1. Among all the tested samples, the LBMH composite with the addition of 7 wt% Nb_2O_5@G yielded the highest dehydrogenation capacity (9.5 wt%) and the shortest dehydrogenation duration (100 min). Therefore, 7 wt% Nb_2O_5@G was identified as the optimal catalyst loading and was selected for further investigation of the catalytic effect of Nb_2O_5@G.

XRD pattern (Fig. 2**a**) exhibited distinct diffraction peaks that were unambiguously assigned to $LiBH_4$ and MgH_2 in the ball-milled composite of $2LiBH_4$-MgH_2 with or without the addition of 7 wt% Nb_2O_5@G. Notably, due to the nanometer size of Nb_2O_5, low crystallinity, and minimal content of Nb_2O_5@G, no detectable diffraction peaks corresponding to Nb_2O_5 or other Nb-related phases were observed in the XRD result of $2LiBH_4$-MgH_2 with the addition of 7 wt% Nb_2O_5@G. The characteristic peaks at 1126, 2221, 2297, and 2390 cm^{-1} in fourier transform infrared spectroscopy (FTIR) [44] further confirm the presence of $LiBH_4$ (Fig. 2**b**). After mixing with 7 wt% Nb_2O_5@G, SEM image of $2LiBH_4$-MgH_2 composite (Fig. 2**c**) revealed a granular morphology with particle diameters on the order of several hundred nanometers. The uniform distribution of Mg of MgH_2, B of $LiBH_4$, and Nb and C of Nb_2O_5@G throughout the sample was confirmed by elemental mapping results, indicating that MgH_2, $LiBH_4$, and Nb_2O_5@G were homogeneously mixed during the ball milling process.

The $2LiBH_4$-MgH_2 composite with the addition of 7 wt% Nb_2O_5@G was subjected to isothermal hydrogen desorption tests at 400 °C and 4 bar hydrogen back pressure, with the addition of commercial Nb_2O_5 (C-Nb_2O_5) included for comparison (Fig. 3**a**). In the case of pure $2LiBH_4$-MgH_2 composite, after the rapid decomposition of MgH_2, the incubation time for MgB_2 formation was about 300 min, and the total hydrogen desorbed reached 10.7 wt%, which is close to the theoretical hydrogen release capacity. In comparison, the LBMH catalyzed by commercial Nb_2O_5 required a longer incubation time. On the other hand, after the addition of Nb_2O_5@G, complete hydrogen release with negligible incubation time for MgB_2 formation was achieved for $2LiBH_4$-MgH_2 composite within only 125 min. These results suggest that the nanostructured Nb_2O_5 accelerates the formation of MgB_2, thereby promoting faster nucleation.

Isothermal hydrogen desorption tests were then conducted on $2LiBH_4$-MgH_2 composite at various temperatures ranging from 380 °C to 440 °C to investigate the catalytic role of Nb_2O_5@G in improving hydrogen desorption kinetics. As shown in Fig. 3**b**, under Nb_2O_5@G catalysis, LBMH released 6 wt% of hydrogen within only 200 min at 380 °C, whereas ball-milled LBMH required more than 600 min to achieve

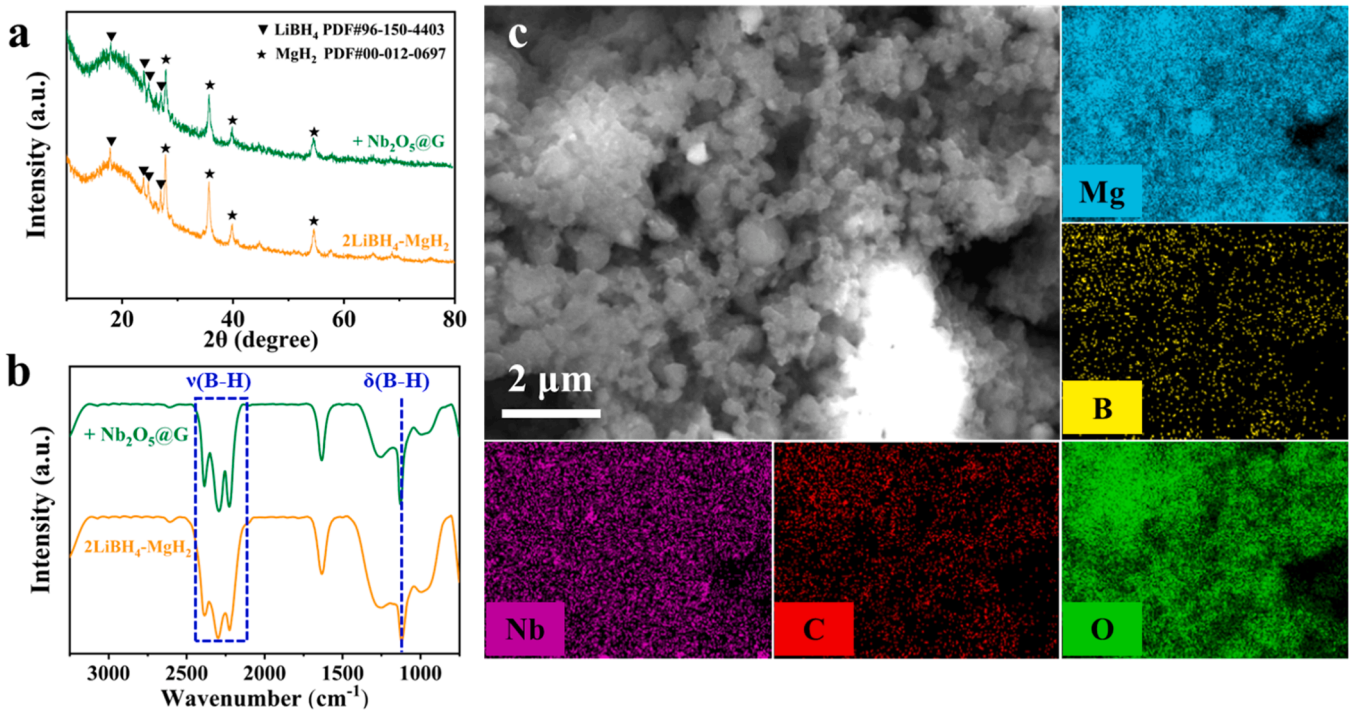

Fig. 2. (a) XRD patterns, (c) FTIR spectra, (d) SEM image and relative EDS mapping images of $2LiBH_4$-MgH_2 composite with the addition of 7 wt% Nb_2O_5@G.

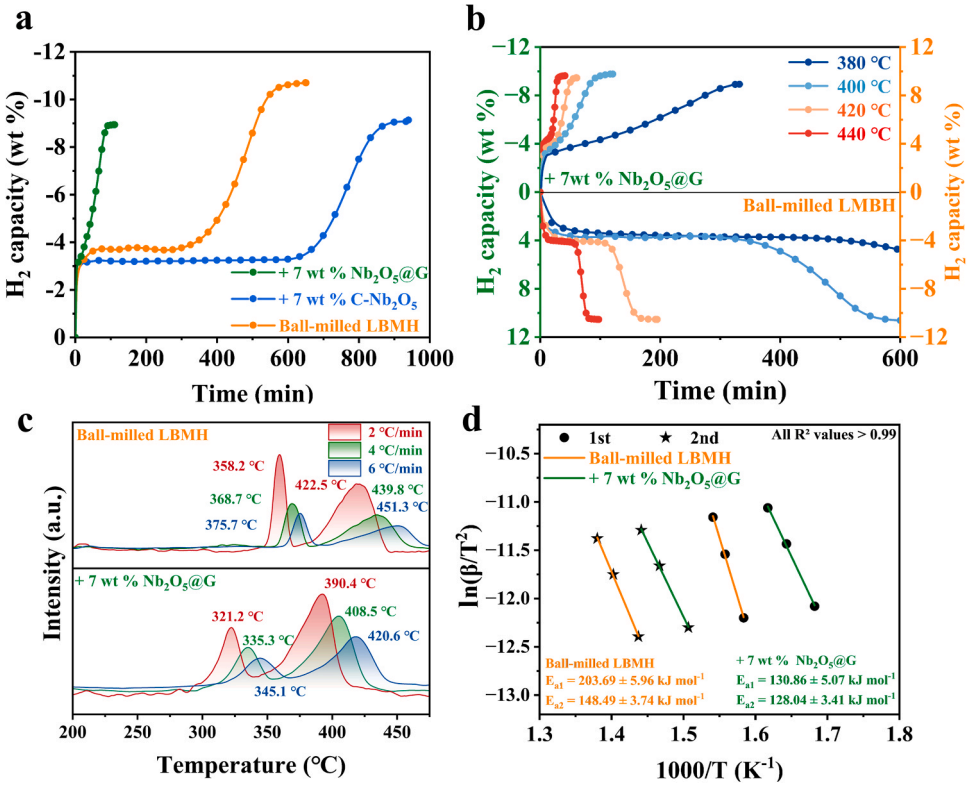

Fig. 3. (a) The isothermal hydrogen desorption curves of LBMH catalyzed by 7 wt% Nb_2O_5@G and 7 wt% commercial Nb_2O_5 at 400 °C and 4 bar hydrogen pressure. (b) Comparison of isothermal hydrogen desorption curves of LBMH before and after the addition of 7 wt% Nb_2O_5@G under 4 bar hydrogen pressure at 380, 400, 420, and 440 °C. (c) Hydrogen desorption rates of LBMH with and without 7 wt% Nb_2O_5@G at different heating rates, and (d) Kissinger plots derived from the desorption data.

the same desorption amount. As the temperature increased, the hydrogen desorption kinetics were significantly enhanced. At 400 °C, the time required for complete desorption was reduced to only 125 min, and upon increasing the operating temperature to 420 °C and 440 °C, the desorption time was further reduced to below 50 min. In contrast, the LBMH sample without a catalyst required 10 h for complete

desorption at 400 °C, with an extended incubation period of 6 h.

In order to quantitatively investigate the positive role of Nb_2O_5@G in improving hydrogen desorption kinetics of 2$LiBH_4$-MgH_2 composite, the apparent activation energy of the reaction was estimated by the Kissinger method based on the hydrogen desorption performance at different heating rates under vacuum (Fig. 3c) according to Eq. (3):

$$\ln(\beta/T_p^2) = -E_a/RT_p + \ln(AR/E_a) \quad (3)$$

where β is the heating rate, T_p is the hydrogen desorption peak at a different heating rate, E_a is the apparent activation energy, R is the gas constant, and A is the pre-exponential factor. The peak desorption temperature (T_P) of 2$LiBH_4$-MgH_2 composite under the catalysis of Nb_2O_5@G is shown in Fig. 3**c**, where a significant reduction in T_p is observed. The relationship between $\ln(\beta/T_p^2)$ and the inverse of T_p was plotted using the Kissinger equation, as shown in Fig. 3d. From the slope of the fitting line, the activation energies (E_a) for the decomposition of MgH_2 and $LiBH_4$ in LBMH were determined to be (203.69 ± 5.96) kJ·mol^{-1} and (148.49 ± 3.74) kJ·mol^{-1}, respectively. In contrast, under the catalysis of Nb_2O_5@G, E_a is significantly decreased to (130.86 ± 5.07) and (128.04 ± 3.41) kJ mol^{-1}, which are 72.83 and 20.45 kJ mol^{-1} lower than that of ball-milled 2$LiBH_4$-MgH_2 composite, respectively. To better illustrate the changes in reaction kinetics under reversible conditions, hydrogen desorption rates for 2$LiBH_4$-MgH_2 composite were also tested under 4 bar hydrogen pressure (Fig. S2). The E_a for the 2$LiBH_4$-MgH_2 composite under the catalysis of Nb_2O_5@G were significantly reduced to (283.51 ± 8.72) kJ·mol^{-1} and (216.82 ± 4.82) kJ·mol^{-1}, which is 24.52 kJ·mol^{-1} and 55.28 kJ·mol^{-1} lower than that of 2$LiBH_4$-MgH_2 composite without the addition of Nb_2O_5@G. This result indicates that, under 4 bar hydrogen pressure, Nb_2O_5 exhibits a better catalytic effect compared to vacuum conditions. The application of 4 bar hydrogen pressure during hydrogen desorption facilitates the reaction between $LiBH_4$ and Mg, thereby leading to the effective formation of MgB_2. This suggests the potential of Nb_2O_5@G is able to promote the nucleation and formation of MgB_2, which in turn could enhance the hydrogen desorption of 2$LiBH_4$-MgH_2 composite.

To evaluate the cycling reversibility of 2$LiBH_4$-MgH_2 composite under the catalysis of Nb_2O_5@G, hydrogen desorption was conducted at 400 °C under 4 bar H_2, followed by hydrogen absorption at 350 °C under 60 bar H_2 for 3 h. The hydrogen desorption curves over the initial 10 cycles are shown in Fig. 4**a**. The Nb_2O_5@G-catalyzed LBMH system exhibited improved dehydrogenation kinetics in the second cycle, with the hydrogen release time decreasing from 125 min (first cycle) to 110 min. From the third cycle, the desorption curves remained largely unchanged, suggesting consistent and reliable catalytic performance. After 10 cycles, the hydrogen storage capacity stabilized at 9.3 wt%, with a minor loss of only 0.2 wt% compared to the first cycle.

For comparison, we also evaluated the cycling performance of the commercial Nb_2O_5 catalyzed 2$LiBH_4$-MgH_2 composite (Fig. S3) and the ball-milled 2$LiBH_4$-MgH_2 composite (Fig. 4**b**) under identical desorption conditions, with the hydrogen absorption time being extended to 8 h. It is noticed that the ball-milled 2$LiBH_4$-MgH_2 composite demonstrated enhanced performance following the initial cycle, a phenomenon that may be attributed to the presence of residual MgB_2 from the hydrogenation step. This residual MgB_2 has been suggested to function as the nucleation site, thereby facilitating the acceleration of hydrogen desorption. However, it still required over 5 h for complete hydrogen desorption during the third cycle. Similarly, the 2$LiBH_4$-MgH_2 composite under the catalysis of commercial Nb_2O_5 required a longer hydrogenation time to maintain stable capacity without degradation. Notably, while the commercial Nb_2O_5 catalyzed 2$LiBH_4$-MgH_2 composite required 950 min for complete hydrogen release during the first cycle, the desorption time decreased significantly in subsequent cycles, stabilizing at approximately 300 min after the third cycle (Fig. S4). This

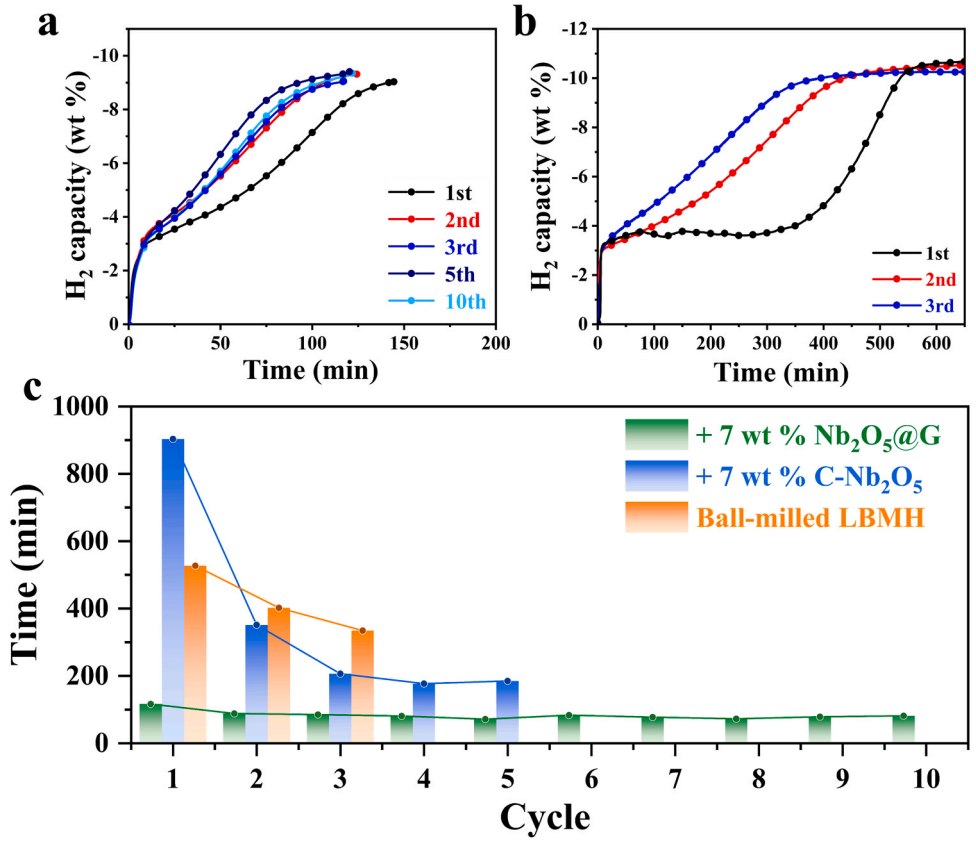

Fig. 4. (a) Reversible dehydrogenation curves of LBMH catalyzed by 7 wt% Nb_2O_5@G. (b) Reversible dehydrogenation curves of LBMH. (c) Time required to reach 90 % of the maximum hydrogen desorption observed in experiments.

suggests that additional reaction time is necessary for the transformation of active catalytic species in the commercial Nb_2O_5 system.

As shown in Fig. 4**c**, the time required to reach 90 % of the full hydrogen capacity during cycling demonstrates the superior performance of Nb_2O_5@G. Across all 10 cycles, the desorption time for $2LiBH_4$-MgH_2 composite under the catalysis of Nb_2O_5@G remained below 90 min. In strong contrast, $2LiBH_4$-MgH_2 composite without and with the addition of commercial Nb_2O_5 required over three cycles to reduce the MgB_2 nucleation incubation period, and the desorption times to reach 90 % hydrogen capacity exceeded 300 min and 200 min, respectively.

To unravel the active catalytic species of Nb_2O_5@G, XRD analysis was performed to observe the phase changes of $2LiBH_4$-MgH_2 composite under the catalysis of Nb_2O_5@G during cycling (Fig. 5**a**). Unfortunately, due to the low crystallinity and small amount of Nb_2O_5@G, no characteristic peaks of Nb_2O_5 or other Nb-based species were observed in the XRD patterns. Subsequent to ball milling, the hydrogenation process following the initial cycles and 10 cycles of hydrogen desorption led to the discernible emergence of characteristic peaks of MgH_2 and $LiBH_4$. After the first and 10 cycles of dehydrogenation, peaks corresponding to LiH and MgB_2 appeared, in good agreement with the theoretical phase changes of the composite during hydrogen absorption and desorption. Notably, the formation of MgO phases was detected during the second hydrogenation cycle following initial dehydrogenation, with sustained MgO presence observed up to the tenth dehydrogenation cycle, possibly due to the transfer of oxygen from Nb_2O_5 to Mg, which leads to the formation of stable MgO. In addition, previous studies have shown that upon heating, Nb_2O_5 decomposes to form $Mg_xNb_{1-x}O$ solid solutions. The resulting MgO suppresses grain growth [45], while the large unit cell of $Mg_xNb_{1-x}O$ induces cracks in the dense MgO phase, creating pathways for hydrogen diffusion [46,47]. As a result, MgO does not hinder hydrogen absorption and desorption but rather facilitates it. FT-IR spectra shown in Fig. 5**b** confirmed these phase transitions.

After ball milling, hydrogenation, and cycling, the characteristic peaks of $LiBH_4$ were prominent (marked by a red dashed box). After the dehydrogenation of the first cycle, the characteristic peaks of $LiBH_4$ were significantly weakened, appearing as faint signals, likely due to the residual presence of a small amount of undecomposed $LiBH_4$. Upon dehydrogenation, these peaks weakened significantly, indicating partial decomposition of $LiBH_4$. Furthermore, as shown in Fig. S5, after 10 cycles, the morphology of the Nb_2O_5@G-catalyzed composite remains largely unchanged, with no obvious particle aggregation observed. This morphological stability contributes to the excellent cycling performance. Meanwhile, no characteristic peaks of $Li_2B_{12}H_{12}$ were detected throughout the cycling process, indicating the stable reversibility of $LiBH_4$ and explaining the superb cycling stability of the Nb_2O_5@G-catalyzed composite.

To analyze the evolution and catalytic role of Nb in $2LiBH_4$-MgH_2 composite under the catalysis of Nb_2O_5@G, XPS analyses of Nb 3*d* and B 1 *s* were conducted at various stages during cycling, as shown in Fig. 5**c**. After ball milling, the deconvoluted Nb 3*d* XPS spectrum exhibited characteristic doublet peaks at 203.4 and 205.6 eV [48], corresponding to NbH_2, and at 204.0 and 206.2 eV, indicative of NbO. The emergence of low-valent Nb in Nb_2O_5 nanoparticles is crucial to accelerating the formation of NbB_2. Additionally, peaks associated with unreduced Nb_2O_5 were observed. In the B 1 s spectrum, peaks corresponding to B-H bonds ($LiBH_4$) and B-O bonds were identified, likely due to minor oxidation of $LiBH_4$ by Nb_2O_5 or during sample preparation and testing. After hydrogen desorption, the Nb 3*d* peaks shifted notably toward lower binding energies, with the disappearance of Nb_2O_5 peaks and the reduction of Nb_2O_5 to NbO_2. New peaks at 203.0 and 204.8 eV [49], combined with a new peak in the B 1 *s* spectrum at 184.7 eV, suggest the formation of NbB_2.

Additionally, a peak at 187.6 eV in the B 1 *s* spectrum corresponds to MgB_2[50], corroborated by XRD results, confirming the successful formation of MgB_2. Notably, after subsequent hydrogenation, the NbB_2 peaks disappeared, while the intensity of NbH_2 peaks increased, and elemental Nb peaks emerged. This indicates the reversible nature of NbB_2 formation, where NbB_2 generated during hydrogen desorption were transformed to NbH_2 and elemental Nb upon hydrogenation. Similarly, the disappearance of MgB_2 peaks after hydrogenation, replaced by B-H peaks, indicates the conversion of MgB_2 back to MgH_2 and $LiBH_4$. The XPS spectra of the sample after 10 cycles were nearly identical to those after the second hydrogenation, suggesting stable

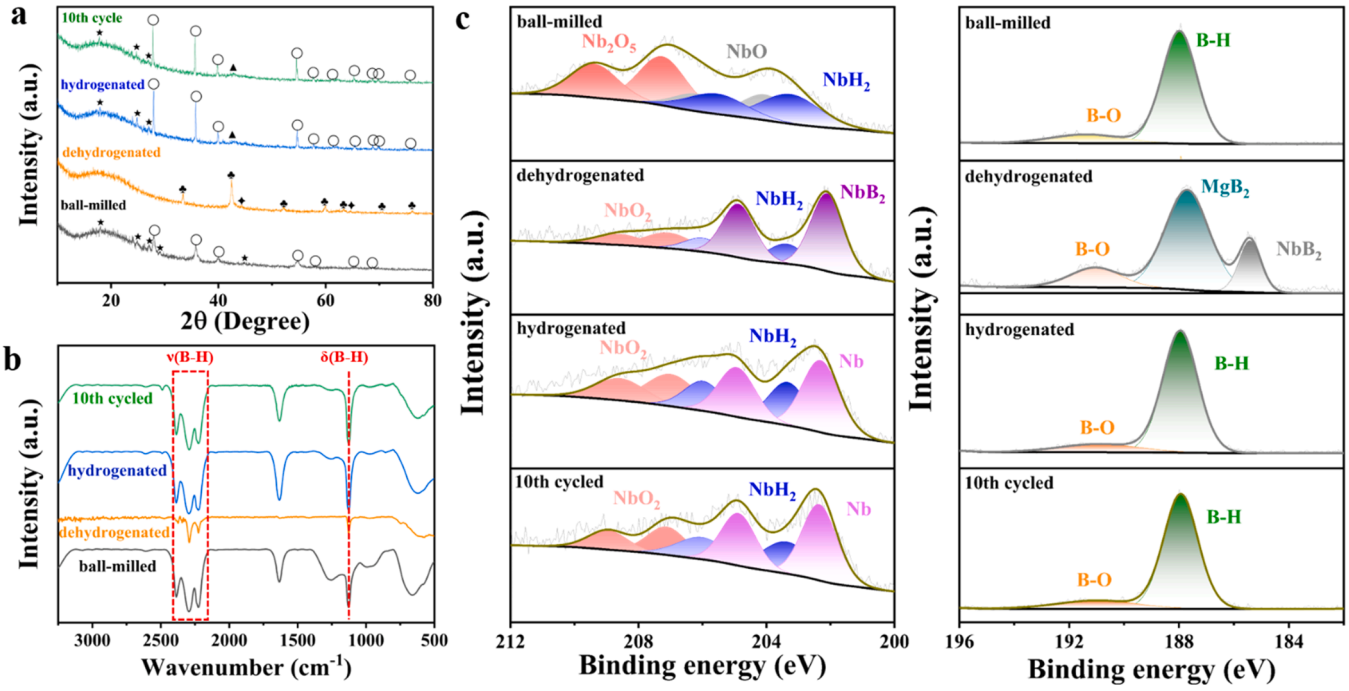

Fig. 5. (a) XRD and (d) FT-IR spectra of LBMH composite catalyzed by 7 wt% Nb_2O_5@G upon cycling. (c) Nb 3*d* and B 1 *s* XPS spectra of LBMH composite catalyzed by 7 wt% Nb_2O_5@G upon cycling.

material composition throughout the cycling process. This stability explains the excellent cyclic performance of the Nb_2O_5@G-catalyzed LBMH composite. These XPS findings align with the proposed catalytic mechanism of Nb_2O_5 in the LBMH system and are consistent with the material transformations observed during cycling.

The decomposition of 2LiBH$_4$-MgH$_2$ composite occurs in two steps. The first step is rapid dehydrogenation of MgH_2 at low temperatures, accompanied by slow dehydrogenation of $LiBH_4$. The second step involving the reaction between Mg and $LiBH_4$ to form MgB_2 is rate-limiting and the formation of MgB_2 is essential for its reversibility. Therefore, a 4-bar H_2 pressure was applied in the reversible hydrogen storage of 2LiBH$_4$-MgH$_2$ composite. Nb_2O_5 was introduced as a catalyst, reacting with $LiBH_4$ to form NdB_2, which serves as a nucleation site for the formation of MgB_2. The catalytic reactions of Nb_2O_5 are shown in Eqs. (4) and (5).

$$2LiBH_4 + Nb_2O_5 \leftrightarrow 2LiBO_2 + NbH_2 + NbO + H_2 \quad (4)$$

$$2LiBH_4 + NbH_2 \leftrightarrow 2LiH + NbB_2 + 4H_2 \quad (5)$$

To further investigate the mechanism of NbB_2 in promoting the nucleation and growth of MgB_2, DFT calculations were conducted to study the epitaxial growth of MgB_2 on Mg and NbB_2 substrates. Typically, during MgB_2 nucleation in 2LiBH$_4$-MgH$_2$ composite, the (110) plane of Mg, with its hexagonal arrangement similar to the Mg layer of MgB_2, facilitates the formation of MgB_2 *via* the interaction of B atoms from $[BH_4]^-$ groups. Under the catalysis of Nb_2O_5, NbB_2 forms as a byproduct in advance through the interaction with B atoms. Both NbB_2 and MgB_2 are intercalation compounds consisting of alternating metallic and B layers, allowing MgB_2 growth to proceed epitaxially on NbB_2 instead of solely relying on *in-situ* MgB_2 nucleation. To evaluate the nucleation tendency of MgB_2, the formation energy was calculated by adding a single layer of Mg or B onto the surface. The specific calculation formula is as follows:

$$E_{formation} = E_{AB} - E_A - E_B \quad (6)$$

where $E_{formation}$ is the formation energy, E_{AB} is the total energy after nucleating a Mg or B layer on the substrate, E_A is the energy of the substrate, and E_B is the energy of the isolated Mg or B layer. DFT calculations (Fig. 6**a**) reveal that the formation of a B layer on NbB_2's Nb layer is thermodynamically more favorable than on Mg, with an energy difference of 75.96 kJ mol^{-1}. Similarly, the subsequent formation of Mg layer is 27.42 kJ mol^{-1} lower in energy on NbB_2 than on Mg. This significant difference arises from the lattice parameter mismatch (Fig. 6**b**). The *d*-value mismatch between NbB_2 and MgB_2 is only 1.6 %, far lower than the 3.5 % mismatch between Mg and MgB_2. Consequently, Mg (110) requires more energy to undergo lattice distortion for B-layer formation. Moreover, the *d*-band electrons of Nb exhibit better orbital overlap with the *p*-orbitals of the B layer, which further reduces the energy required for nucleation, as shown in Fig. S6. The thermodynamic advantage of NbB_2 in the growth of Mg and B layers alters the nucleation pathway of MgB_2, accelerating the decomposition kinetics of $LiBH_4$. In summary, the rapid formation of nanostructured MgB_2, facilitated by the low formation energy of Mg and B on the NbB_2 surface, enables 2LiBH$_4$-MgH$_2$ composite the shortest desorption time compared to previously reported results (Table S1).

4. Conclusion

In summary, this work synthesized graphene-wrapped nano-Nb_2O_5 (Nb_2O_5@G) as a catalyst for the 2LiBH$_4$-MgH$_2$ composite hydrogen storage material. Experimental results demonstrated that the addition of 7 wt% Nb_2O_5@G significantly enhanced hydrogen storage performance of 2LiBH$_4$-MgH$_2$ composite. During the first dehydrogenation at 400 °C, the Nb_2O_5@G-catalyzed system released 9.5 wt% H_2 within just 125 min, compared to 900 min for the system catalyzed by 7 wt% commercial Nb_2O_5. Furthermore, the Nb_2O_5@G-catalyzed 2LiBH$_4$-MgH$_2$ composite maintains complete dehydrogenation within 90 min and a stable hydrogen capacity of 9.3 wt% over the subsequent 9 cycles with negligible degradation, thus achieving high-capacity reversible hydrogen storage of 2LiBH$_4$-MgH$_2$ composite. During the dehydrogenation process, the *in-situ* formed NbB_2 acted as a nucleation site for MgB_2, significantly reducing the induction time and accelerating nucleation rates, which thereby shortens the dehydrogenation time and improves the reversible hydrogen storage performance of the composite.

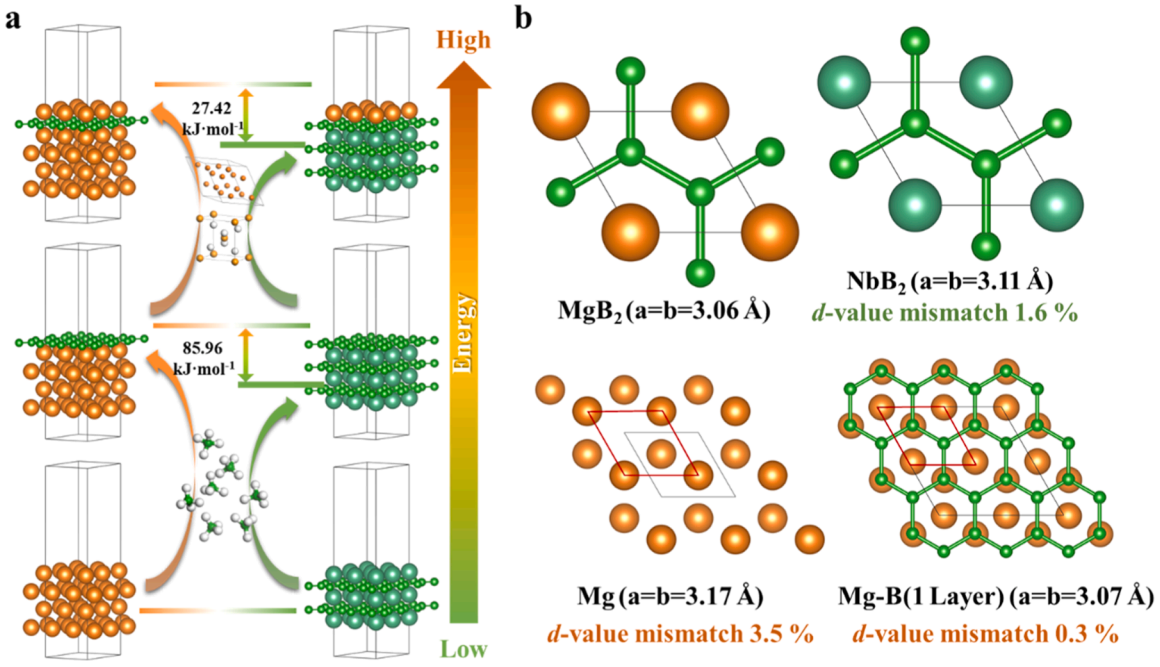

Fig. 6. (a) Comparison of formation energy changes between Mg and NbB_2 in forming alternating B and Mg layers during MgB_2 nucleation. (b) Lattice parameters of MgB_2, NbB_2, Mg, and Mg covered with a single B layer. Orange and green large spheres represent Mg and Nb atoms, respectively, while small green spheres represent B atoms.

Theoretical calculations revealed that the formation energies of B and Mg layers during MgB_2 nucleation are reduced by 85.96 $kJ{\cdot}mol^{-1}$ and 27.42 $kJ{\cdot}mol^{-1}$, respectively, due to the minimal 1.6 % *d*-value mismatch between NbB_2 and MgB_2, which greatly accelerates the dehydrogenation rate of $LiBH_4$. Additionally, the nanoscale structure of Nb_2O_5 facilitated its rapid reaction with B to form NbB_2, which facilitates the formation of MgB_2 and thereby reduces the dehydrogenation temperature of $2LiBH_4$-MgH_2 composite. This study demonstrates the potential of low lattice mismatch metal borides as nucleation sites for the formation of MgB_2. This approach provides a novel and effective strategy for optimizing the hydrogen storage performance of reactive hydride composites.

CRediT authorship contribution statement

Xuechun Hu: Validation, Investigation, Data curation. **Guanglin Xia:** Writing – review & editing, Supervision, Resources, Methodology, Investigation, Funding acquisition, Formal analysis, Conceptualization. **Ying Ding:** Writing – original draft, Supervision, Methodology, Investigation, Conceptualization. **Xiaoyue Zhang:** Writing – original draft, Validation, Supervision. **Chaoqun Li:** Writing – original draft, Software, Methodology, Data curation, Conceptualization.

Declaration of Competing Interest

The authors declare that they have no known competing financial interests or personal relationships that could have appeared to influence the work reported in this paper.

Acknowledgments

This work was partially supported by the National Key R&D Program of China (No. 2021YFB3802400), the National Natural Science Foundation of China (No. U2130208 and 22279020), and the Science and Technology Commission of Shanghai Municipality (No. 23ZR1406500).

Appendix A. Supporting information

Supplementary data associated with this article can be found in the online version at doi:10.1016/j.jallcom.2025.183052.

References

[1] A.P. Zhao, S. Li, D. Xie, Y. Wang, Z. Li, P.J.-H. Hu, Q. Zhang, Hydrogen as the nexus of future sustainable transport and energy systems, Nat. Rev. Electr. Eng. 2 (2025) 447–466.
[2] N. Johnson, M. Liebreich, D.M. Kammen, P. Ekins, R. McKenna, I. Staffell, Realistic roles for hydrogen in the future energy transition, Nat. Rev. Clean. Technol. 1 (2025) 351–371.
[3] N. Kumar, S.-Y. Lee, S.-J. Park, Advancements in hydrogen storage technologies: a comprehensive review of materials, methods, and economic policy, Nano Today 56 (2024) 102302.
[4] H. Sun, Z. Wang, Q. Meng, S. White, Advancements in hydrogen storage technologies: enhancing efficiency, safety, and economic viability for sustainable energy transition, Int. J. Hydrog. Energy 105 (2025) 10–22.
[5] Y. Xu, Y. Zhou, Y. Li, Z. Ding, Research progress and application prospects of Solid-State hydrogen storage technology, Molecules 29 (2024) 1767.
[6] X. Zhang, C. Li, J. Ye, X. Hu, W. Chen, F. Fang, D. Sun, Y. Liu, X. Yu, G. Xia, Light-Enabled reversible hydrogen storage of borohydrides activated by photogenerated vacancies, J. Am. Chem. Soc. 147 (2025) 2786–2796.
[7] X. Hu, X. Chen, X. Zhang, Y. Meng, G. Xia, X. Yu, D. Sun, F. Fang, In situ construction of interface with photothermal and mutual catalytic effect for efficient solar-driven reversible hydrogen storage of MgH_2, Adv. Sci. 11 (2024) 2400274.
[8] S. Shen, Y. Li, L. Ouyang, L. Zhang, M. Zhu, Z. Liu, V–Ti-Based solid solution alloys for Solid-State hydrogen storage, Nano Micro. Lett. 17 (2025) 1–30.
[9] M. Altaf, U. Demirci, A. Haldar, Review of solid-state hydrogen storage: materials categorisation, recent developments, challenges and industrial perspectives, Energy Rep. 13 (2025) 5746–5772.
[10] W. Grochala, P.P. Edwards, Thermal decomposition of the non-interstitial hydrides for the storage and production of hydrogen, Chem. Rev. 104 (2004) 1283–1316.
[11] C. Liu, Z. Yuan, X. Li, Y. Sun, T. Zhai, Z. Han, L. Zhang, T. Li, Review on improved hydrogen storage properties of MgH_2 by adding new catalyst, J. Energy Storage 97 (2024) 112786.
[12] C. Zheng, B. Liu, D. Zhou, Z. Hou, D. Zhao, A systematic review on nanostructure engineering of Mg/MgH_2 for enhanced hydrogen storage performance, Int. J. Hydrog. Energy 160 (2025) 150629.
[13] Z. Huo, Q. Wu, H. Li, Y. Zhang, K. Chen, D. Shi, Recent advances in modification methods for $LiBH_4$-Based hydrogen storage materials, J. Alloy. Compd. 1037 (2025) 182370.
[14] W. Zhang, X. Zhang, Z. Huang, H.-W. Li, M. Gao, H. Pan, Y. Liu, Recent development of lithium borohydride-based materials for hydrogen storage, Adv. Energy Sustain. Res. 2 (2021) 2100073.
[15] U. Bösenberg, S. Doppiu, L. Mosegaard, G. Barkhordarian, N. Eigen, A. Borgschulte, T.R. Jensen, Y. Cerenius, O. Gutfleisch, T. Klassen, Hydrogen sorption properties of MgH_2–$LiBH_4$ composites, Acta Mater. 55 (2007) 3951–3958.
[16] J.J. Vajo, S.L. Skeith, F. Mertens, Reversible storage of hydrogen in destabilized $LiBH_4$, J. Phys. Chem. B 109 (2005) 3719–3722.
[17] U. Bösenberg, J.W. Kim, D. Gosslar, N. Eigen, T.R. Jensen, J.B. Von Colbe, Y. Zhou, M. Dahms, D. Kim, R. Günther, Role of additives in $LiBH_4$–MgH_2 reactive hydride composites for sorption kinetics, Acta Mater. 58 (2010) 3381–3389.
[18] Y. Liu, H. Du, X. Zhang, Y. Yang, M. Gao, H. Pan, Superior catalytic activity derived from a two-dimensional Ti_3C_2 precursor towards the hydrogen storage reaction of magnesium hydride, Chem. Commun. 52 (2016) 705–708.
[19] S. Shen, W. Liao, Z. Cao, J. Liu, H. Wang, L. Ouyang, Enhanced hydrogen storage properties of MgH_2 with the co-addition of $LiBH_4$ and YNi_5 alloy, J. Mater. Sci. Technol. 178 (2024) 90–99.
[20] P. Gao, X. Zhang, X. Hu, X. Yu, D. Sun, F. Fang, G. Xia, Li/Mg-Based hydrides for High-Capacity hydrogen and lithium storage applications, Adv. Funct. Mater. (2025) 2425155.
[21] W. Chen, Y.-H. Sun, T. Xu, X.-B. Yu, G.-L. Xia, Enhancing reversible hydrogen storage performance of $2LiBH_4$–MgH_2 via in-situ building heterogeneous nucleation sites, Rare Met. 43 (2024) 4367–4376.
[22] J. Jepsen, C. Milanese, J. Puszkiel, A. Girella, B. Schiavo, G.A. Lozano, G. Capurso, J.M. Bellosta von Colbe, A. Marini, S. Kabelac, Fundamental material properties of the $2LiBH_4$-MgH_2 reactive hydride composite for hydrogen storage:(I) thermodynamic and heat transfer properties, Energies 11 (2018) 1081.
[23] F. Karimi, M.V. Riglos, A. Santoru, A. Hoell, V.S. Raghuwanshi, C. Milanese, N. Bergemann, C. Pistidda, P. Nolis, M.D. Baro, In situ formation of TiB_2 nanoparticles for enhanced dehydrogenation/hydrogenation reaction kinetics of $LiBH_4$–MgH_2 as a reversible solid-state hydrogen storage composite system, J. Phys. Chem. C. 122 (2018) 11671–11681.
[24] K. Wang, X. Kang, Q. Kang, Y. Zhong, C. Hu, P. Wang, Improved reversible dehydrogenation of $2LiBH_4$–MgH_2 composite by the controlled formation of transition metal boride, J. Mater. Chem. A 2 (2014) 2146–2151.
[25] Y.-K. Liu, Y.-C. Pang, C.-Q. Li, X.-Y. Zhang, X.-C. Hu, W. Chen, X.-B. Yu, G.-L. Xia, Amorphous VB_2 nanoparticles for stable hydrogen storage of $2LiBH_4$–MgH_2, Rare Met 44 (2025) 5544–5553.
[26] L.-W. Lu, H. Luo, G.-X. Li, Y. Li, X.-H. Wang, C.-K. Huang, Z.-Q. Lan, W.-Z. Zhou, J. Guo, M. Ismail, Layered niobium carbide enabling excellent kinetics and cycling stability of Li-Mg-BH hydrogen storage material: layered niobium carbide enabling excellent kinetics, Rare Met 43 (2024) 1153–1166.
[27] Y. Jia, P. Zhou, X. Xiao, X. Wang, B. Han, J. Wang, F. Xu, L. Sun, L. Chen, Synergetic action of 0D/2D/3D N-doped carbon nanocages and NbB_2 nanocatalyst on reversible hydrogen storage performance of lithium borohydride, Chem. Eng. J. 485 (2024) 150090.
[28] X. Zhang, Y. Liu, Z. Ren, X. Zhang, J. Hu, Z. Huang, Y. Lu, M. Gao, H. Pan, Realizing 6.7 wt% reversible storage of hydrogen at ambient temperature with non-confined ultrafine magnesium hydrides, Energy Environ. Sci. 14 (2021) 2302–2313.
[29] Y. Pang, Y. Liu, M. Gao, L. Ouyang, J. Liu, H. Wang, M. Zhu, H. Pan, A mechanical-force-driven physical vapour deposition approach to fabricating complex hydride nanostructures, Nat. Commun. 5 (2014) 3519.
[30] Y. Liu, K. Zhong, K. Luo, M. Gao, H. Pan, Q. Wang, Size-dependent kinetic enhancement in hydrogen absorption and desorption of the Li−Mg−N−H system, J. Am. Chem. Soc. 131 (2009) 1862–1870.
[31] F. Güleç, W. Oakley, X. Liu, S. Nayebossadri, F. Wang, E.K. Smith, S.M. Barakat, E. H. Lester, Status and progress of nanomaterials application in hydrogen storage, Nanomater. Sustain. Hydrog. Prod. Storage (2024) 136–165.
[32] X. Fan, X. Xiao, L. Chen, X. Wang, S. Li, H. Ge, Q. Wang, High catalytic efficiency of amorphous TiB_2 and NbB_2 nanoparticles for hydrogen storage using the $2LiBH_4$–MgH_2 system, J. Mater. Chem. A 1 (2013) 11368–11375.
[33] Y. Wang, X. Chen, H. Zhang, G. Xia, D. Sun, X. Yu, Heterostructures built in metal hydrides for advanced hydrogen storage reversibility, Adv. Mater. 32 (2020) 2002647.
[34] G. Xia, Y. Tan, X. Chen, D. Sun, Z. Guo, H. Liu, L. Ouyang, M. Zhu, X. Yu, Monodisperse magnesium hydride nanoparticles uniformly self-assembled on graphene, Adv. Mater. 27 (2015) 5981–5988.
[35] H. Zhang, G. Xia, J. Zhang, D. Sun, Z. Guo, X. Yu, Graphene-Tailored thermodynamics and kinetics to fabricate metal borohydride nanoparticles with high purity and enhanced reversibility, Adv. Energy Mater. 8 (2018) 1702975.
[36] D. Khan, W.J. Ong, Tailoring hydrogen storage materials kinetics and thermodynamics through nanostructuring, and nanoconfinement with In-Situ catalysis, Interdiscip. Mater. 4 (2025) 249–283.
[37] P.E. Blöchl, Projector augmented-wave method, Phys. Rev. B 50 (1994) 17953.
[38] J. Wellendorff, T.L. Silbaugh, D. Garcia-Pintos, J.K. Nørskov, T. Bligaard, F. Studt, C.T. Campbell, A benchmark database for adsorption bond energies to transition metal surfaces and comparison to selected DFT functionals, Surf. Sci. 640 (2015) 36–44.
[39] J.P. Perdew, K. Burke, M. Ernzerhof, Generalized gradient approximation made simple, Phys. Rev. Lett. 77 (1996) 3865.

[40] C. Li, W. Yang, H. Liu, X. Liu, X. Xing, Z. Gao, S. Dong, H. Li, Picturing the gap between the performance and US-DOE's hydrogen storage target: a Data-Driven model for MgH_2 dehydrogenation, Angew. Chem. Int. Ed. 63 (2024) e202320151.
[41] S. Grimme, J. Antony, S. Ehrlich, H. Krieg, A consistent and accurate ab initio parametrization of density functional dispersion correction (DFT-D) for the 94 elements H-Pu, J. Chem. Phys. 132 (2010) 154104.
[42] S. Tamura, K. Kato, M. Goto, Single crystals of T-Nb_2O_5 obtained by slow cooling method under high pressures, Z. Anorg. Allg. Chem. 410 (1974) 313–315.
[43] P. Carniti, A. Gervasini, M. Marzo, Dispersed NbO_x catalytic phases in silica matrixes: influence of niobium concentration and preparative route, J. Phys. Chem. C. 112 (2008) 14064–14074.
[44] J. Zhu, H. Wang, W. Cai, J. Liu, L. Ouyang, M. Zhu, The milled $LiBH_4$/h-BN composites exhibiting unexpected hydrogen storage kinetics and reversibility, Int. J. Hydrog. Energy 42 (2017) 15790–15798.
[45] O. Friedrichs, F. Agueyzinsou, J. Fernandez, J. Sanchezlopez, A. Justo, T. Klassen, R. Bormann, A. Fernandez, MgH_2 with Nb_2O_5 as additive, for hydrogen storage: chemical, structural and kinetic behavior with heating, Acta Mater. 54 (2006) 105–110.
[46] T.K. Nielsen, T.R. Jensen, MgH_2–Nb_2O_5 investigated by in situ synchrotron X-ray diffraction, Int. J. Hydrog. Energy 37 (2012) 13409–13416.
[47] R.A. Ocampo, J. Arias-Velandia, J.A. Lenis, A.A.Z. Gil, S. Bello, E. Correa, C. Arrieta, F.J. Bolívar, F. Echeverria Echeverria, Microwave-assisted synthesis of MgH_2 nanoparticles for hydrogen storage applications, Nanopart. Hydrog. Storage Appl. J. Nanopart. Res 27 (2025) 52.
[48] Y. Meng, S. Ju, W. Chen, X. Chen, G. Xia, D. Sun, X. Yu, Design of bifunctional Nb/V interfaces for improving reversible hydrogen storage performance of MgH_2, Small Struct. 3 (2022) 2200119.
[49] R. Escamilla, L. Huerta, X-ray photoelectron spectroscopy studies of non-stoichiometric superconducting NbB_{2+x}, Supercond. Sci. Technol. 19 (2006) 623.
[50] A. Talapatra, S. Bandyopadhyay, P. Sen, P. Barat, S. Mukherjee, M. Mukherjee, X-ray photoelectron spectroscopy studies of MgB_2 for valence state of mg, Phys. C. 419 (2005) 141–147.